

Single-Crystal Nitrogen-Rich Two-Dimensional Mo_5N_6 Nanosheets for Efficient and Stable Seawater Splitting

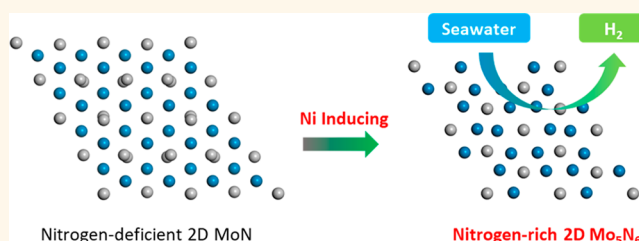
Huanyu Jin, Xin Liu, Anthony Vasileff, Yan Jiao,^{1b} Yongqiang Zhao, Yao Zheng,^{1b} and Shi-Zhang Qiao^{1b}

School of Chemical Engineering, The University of Adelaide, Adelaide, SA 5005, Australia

S Supporting Information

ABSTRACT: Transition metal nitrides (TMNs) have great potential for energy-related electrocatalysis because of their inherent electronic properties. However, incorporating nitrogen into a transition metal lattice is thermodynamically unfavorable, and therefore most of the developed TMNs are deficient in nitrogen. Consequently, these TMNs exhibit poor structural stability and unsatisfactory performance for electrocatalytic applications. In this work, we design and synthesize an atomically thin nitrogen-rich nanosheets, Mo_5N_6 , with the help of a Ni-inducing growth method. The as-prepared single-crystal electrocatalyst with abundant metal–nitrogen electroactive sites displays outstanding activity for the hydrogen evolution reaction (HER) in a wide range of electrolytes (pH 0–14). Further, the two-dimensional Mo_5N_6 nanosheets exhibit high HER activity and stability in natural seawater that are superior to other TMNs and even the Pt benchmark. By combining synchrotron-based spectroscopy and the calculations of electron density of state, we find that the enhanced properties of these nitrogen-rich Mo_5N_6 nanosheets originates from its Pt-like electronic structure and the high valence state of its Mo atoms.

KEYWORDS: 2D materials, nitrogen-rich, metal nitrides, hydrogen evolution, seawater splitting



Hydrogen is a promising energy carrier for clean energy systems because it has a high energy density and can be produced using renewable energy.^{1–3} To produce high-purity hydrogen, water electrolysis is superior to current methods, such as natural gas reforming or coal gasification, which require extensive processing and energy.^{4–6} Seawater is the most abundant water source and natural electrolyte on the earth, which makes it very suitable for low-cost and large-scale hydrogen production.⁷ However, compared to the hydrogen evolution reaction (HER) in acid or alkaline media, electrocatalytic HER in natural seawater is extremely challenging due to its intrinsic low conductivity, ion poisoning, and high corrosivity.^{7–9} For example, Pt exhibits outstanding HER performance in conventional water electrolysis systems but poor performance in seawater conditions due to the poisoning effects from a range of undesirable anions.

Recently, transition metal nitrides (TMNs) have emerged as promising electrocatalyst materials for various electrocatalytic processes (e.g., HER, oxygen evolution reaction, oxygen reduction reaction, and so forth).^{5,10–14} Because of their inherent electronic structure and good electrical conductivity, TMNs could potentially replace noble metal catalysts for water splitting.^{13,15–17} However, most TMNs are vulnerable to oxidation during electrocatalytic processes due to the low

valence state of the metal atoms.¹⁷ This causes them to be relatively unstable. Given this, nitrogen-rich TMNs (N/metal > 1) are preferable for electrocatalysis because of the higher valence state of the metal atoms leading to their better corrosion resistance.^{17–19} However, incorporating nitrogen atoms into the crystalline lattices of transition metals is thermodynamically unfavorable, and they tend to diffuse out of the metal lattice.^{16–18} Therefore, most of the TMNs reported have low nitrogen content with molar ratios of N/metal less than unity (e.g., Ni_3N , Cu_3N , Co_4N , Mo_2N , and so forth).^{17,20}

For various energy related applications, two-dimensional (2D) TMNs have superior performance to their bulk counterpart due to their uniform crystal lattice and tunable electronic structure.^{21–25} Hence, synthesis of nitrogen-rich 2D TMNs with uniform exposure of specific facets would be key to optimizing these electrocatalysts for high performance applications.^{17,26,27} However, the development of nitrogen-rich 2D TMNs is limited by the harsh synthetic conditions required and the inability to control their morphologies well. Recently, Yu et al. realized the synthesis of the nitrogen-rich W_2N_3 under

Received: October 14, 2018

Accepted: November 29, 2018

Published: November 29, 2018



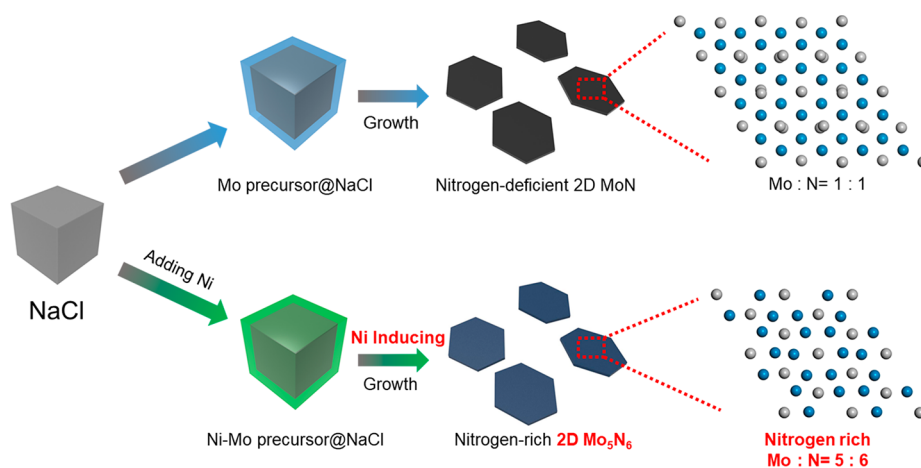


Figure 1. Schematic illustration of the synthesis of MoN and Mo₅N₆ nanosheets through an ammonization synthesis with and without the addition of Ni in the precursor.

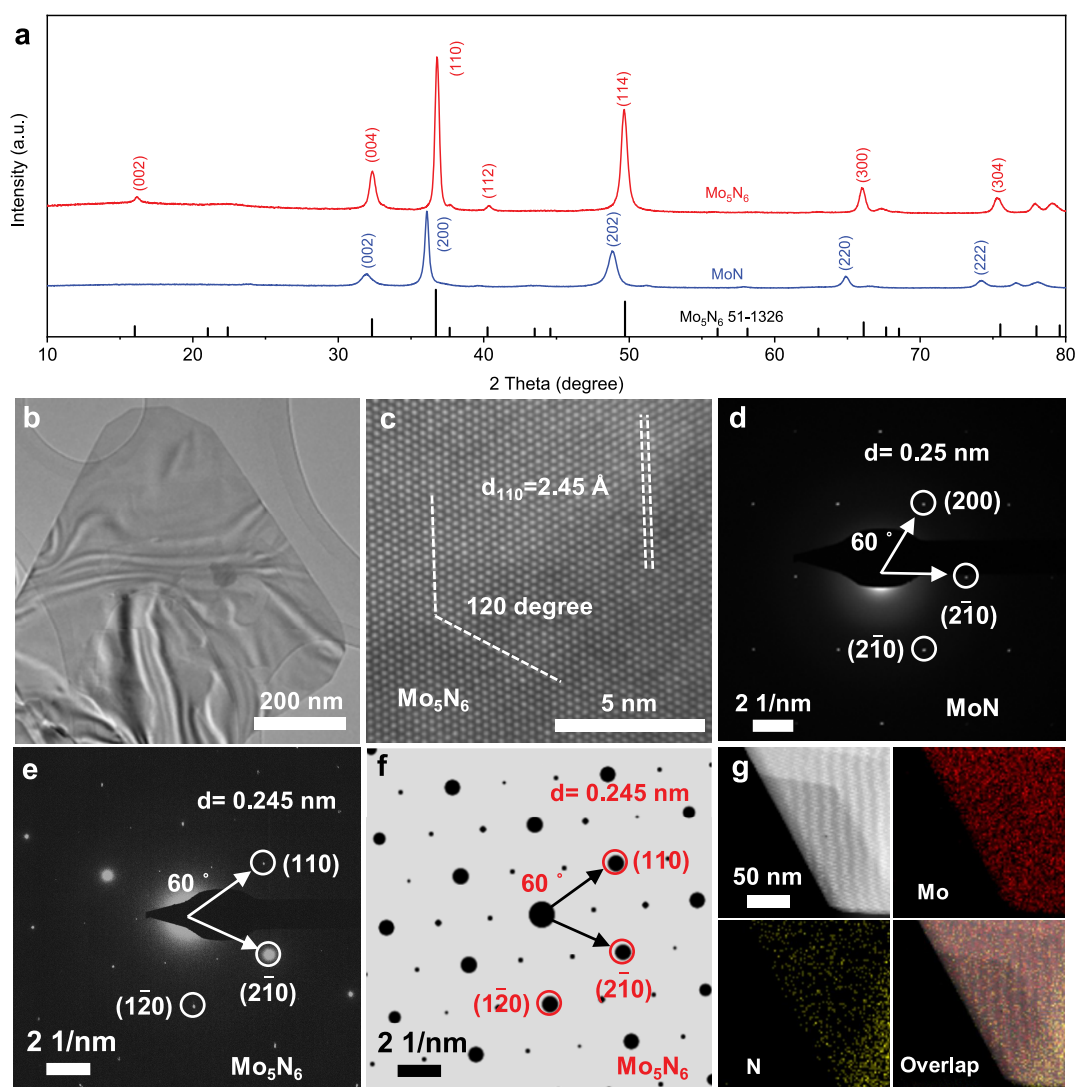


Figure 2. Characterization of Mo₅N₆ and MoN. (a) XRD pattern, (b) low-resolution TEM image, (c) high-resolution STEM image of Mo₅N₆, (d) SAED pattern of MoN, (e,f) SAED patterns and (g) elemental mapping of Mo₅N₆.

atmospheric pressure using salt template method, which would otherwise require higher pressures.²⁸ In the meantime, researchers found that the first row transition metals (e.g.,

Fe, Co and Ni) can induce the transformation of β -WN to anomalous δ -WN under atmospheric pressure.¹¹ In these cases, the transition metal component and salt crystal serve as

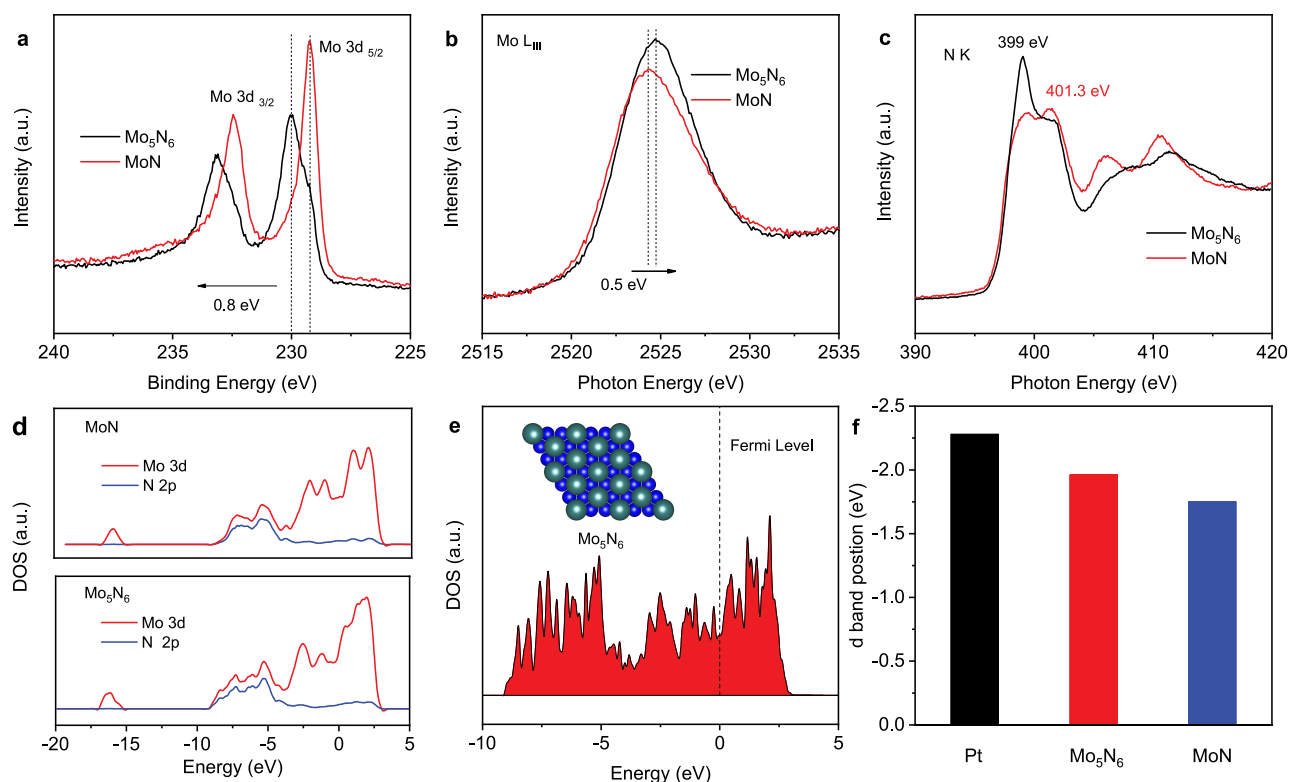


Figure 3. (a) Mo 3d XPS spectra of MoN and Mo_3N_6 . (b) Mo L_{III} edge of MoN and Mo_3N_6 . (c) N K edge of MoN and Mo_3N_6 . (d) DOS of Mo 3d and N 2p orbitals for MoN and Mo_3N_6 . (e) DOS of Mo_3N_6 . (f) d band center position of Pt (111), Mo_3N_6 and MoN , respectively.

the catalyst and template which induce the formation of anomalous metal nitrides. We speculate the same concept is likely suitable for the synthesis of nitrogen-rich TMNs under mild conditions.

In this work, we apply this transition metal-catalyzed phase transformation method with 2D lateral growth methods to synthesize the atomically thin Mo_3N_6 nanosheets. With rich metal-nitrogen bonding, the as-prepared 2D Mo_3N_6 nanosheets show enhanced HER activity compared to conventional nitrogen-deficient TMNs in various electrolytes (pH 0–14). More significantly, Mo_3N_6 exhibits an outstanding HER performance in natural seawater with a highly stable catalytic current over 100 h, which is much better than Pt/C benchmark and other TMNs counterparts. Synchrotron-based X-ray absorption near edge structure (XANES) and the calculations of electron DOS confirm that the high activity of Mo_3N_6 originates from its Pt-like electronic structure, and its stability derives from the high valence state of its Mo atoms which make it relatively unsusceptible to active site poisoning from deleterious seawater ions.

RESULTS AND DISCUSSION

The 2D Mo_3N_6 nanosheets were prepared by a Ni-induced salt-templated method, which is schematically shown in Figure 1.^{21,28–30} First, nickel acetate and $\text{MoO}(\text{OH})_x$ were used as precursors, and the former was reduced to Ni metal by ammonia gas at high temperature (Figure S1a). The Ni metal was then removed by an acid wash which yielded pure phase Mo_3N_6 (Figure S1). It should be noted that without the addition of Ni salt, the final product obtained was regular MoN . From Figure S1b, the O 1s peak is observed which we attributed to oxygen termination on the Mo_3N_6 surface.

Through a comparison of the X-ray diffraction (XRD) patterns, the synthesized Mo_3N_6 possesses the different peak position with that of MoN (Figure 2a), indicating that the extra (20%) nitrogen-incorporation can greatly change the crystal structure of conventional MoN . The 2D morphology of the Mo_3N_6 nanosheets were observed under scanning electron microscope (SEM) and transmission electron microscopy (TEM) imaging, which showed that the nanosheets are transparent and wrinkled (Figure 2b, Figure S2). Furthermore, the Mo_3N_6 nanosheet is only 3 nm thick, demonstrating its atomically thin 2D structure with uniformly exposed lattice and large surface area (Figure S3).

The crystal structure parameters of Mo_3N_6 were determined using aberration-corrected scanning TEM imaging and corresponding selected area electron diffraction (SAED). The scanning TEM image (Figure 2c) shows the hexagonal structure of Mo_3N_6 with an interplanar distance of 2.45 Å for (110) facets, which is smaller than that of 2.5 Å for the (200) facets of MoN (Figure S4). This demonstrates the more compact hexagonal structure of Mo_3N_6 compared to MoN . Moreover, one set of diffraction spots in the SAED image of Mo_3N_6 reveals its single crystalline nature (Figure 2e). We also determine the (110) lattice plane spacing of Mo_3N_6 to be 0.245 nm, consisting with the result of XRD and high-resolution TEM. For MoN , the (200) lattice plane spacing is 0.25 nm, which is larger than that of Mo_3N_6 (Figure 2d), further indicating the different crystal structure of MoN and Mo_3N_6 (Figure 2f). The interplanar angle and distance of the experimental and simulated SAED patterns of Mo_3N_6 (Figure 2f) also match well with one another, demonstrating the pure phase of the Mo_3N_6 . Energy dispersive spectroscopy (EDS) mapping clearly shows the spatial distribution of Mo and N

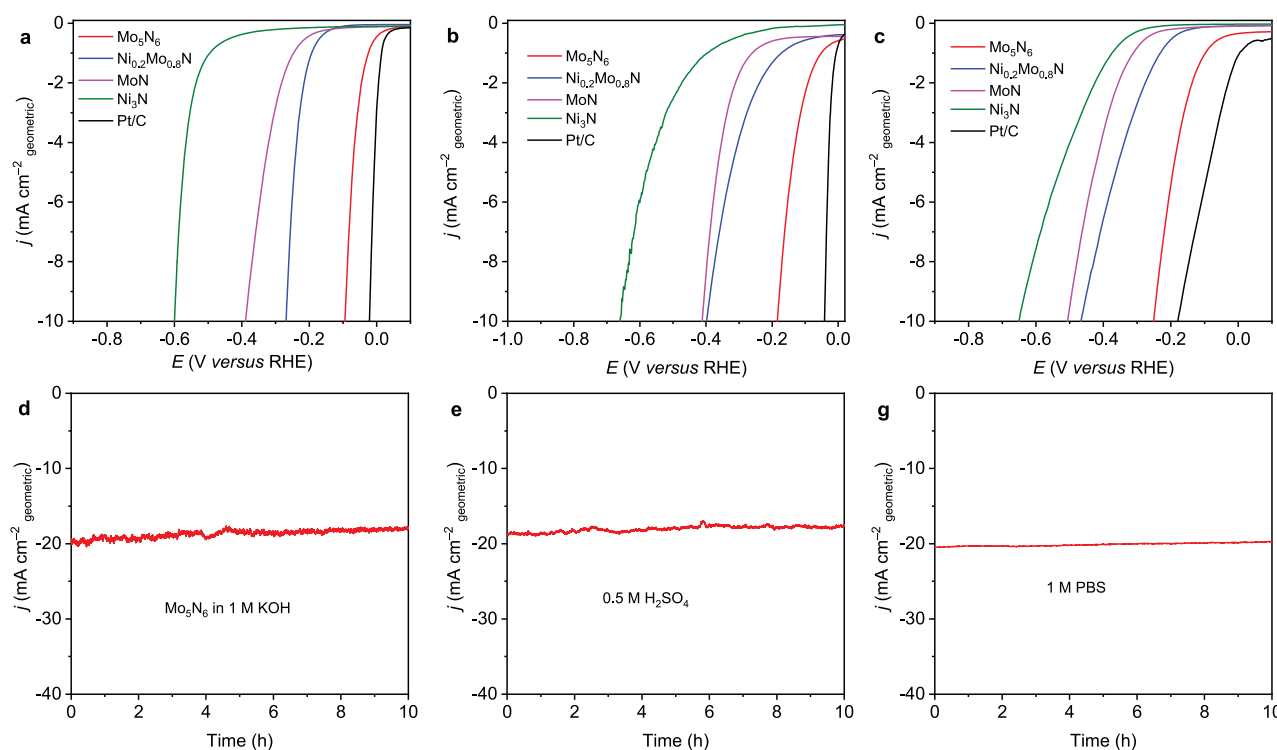


Figure 4. Electrochemical performance of Mo₅N₆ and other catalysts in different electrolytes: (a–c) LSV curves of Mo₅N₆, MoN, Ni_{0.2}Mo_{0.8}N, Ni₃N, and commercial Pt/C electrodes measured in Ar-saturated 1 M KOH, 0.5 M H₂SO₄, and 1 M PBS, respectively. (d–f) Chronoamperometric results of Mo₅N₆ in different electrolytes. The applied potentials for d–f are 130, 230, and 330 mV, respectively.

atoms on the hexagonal corner area and the uniform composition of the synthesized Mo₅N₆ nanosheets (Figure 2g).

We conducted a range of spectroscopic measurements and theoretical calculations to evaluate the electronic structure of Mo₅N₆ at the atomic level, and more importantly, its difference with conventional MoN. As shown in the high-resolution Mo 3d XPS spectra (Figure 3a), the dominant valence state of Mo in Mo₅N₆ is 4+ (binding energy of 230.0 eV), which is higher than that of MoN (+3, binding energy of 229.3 eV). The higher valence state of Mo in Mo₅N₆ is likely due to the greater number of nitrogen atoms in the crystal lattice leading to an increased electron redistribution from Mo to N atoms. The Mo L_{III}-edge XANES spectrum also confirms the higher oxidation state of the Mo cation in Mo₅N₆ than that of MoN (Figure 3b), by identifying a positive energy shift of 0.5 eV. Importantly, according to previous study, Mo (4+) species can facilitate OH* intermediate adsorption during water dissociation, which is critical for HER performance in alkaline media.^{30,31} Other than valence state, periodic Mo vacancies are observed in the molecular structure of Mo₅N₆ (Figure S5), which inevitably changes the metal-nitrogen bonding in the supercell and consequently leads to a different electronic structure. Experimentally, the N K-edge XANES of MoN and Mo₅N₆ are characterized by two sharp resonances at lower energy (399.0 and 401.3 eV) and two broad features at higher energy (405–415 eV). The former two peaks can be assigned to the transitions of N 1s electrons to the p–d(t_{2g}) and p–d(e_g) hybridized orbitals, respectively. The latter two peaks can be assigned to the transition of N 1s electrons to an orbital that involves contributions from 2p and 3p orbitals of nitrogen and the d and s states of Mo.^{32,33} As shown in Figure 3c, the relative peak intensity of Mo₅N₆ at 399.0 eV is stronger than

the peak at 401.3 eV, indicating that more N 1s electrons transfer to the p–d(t_{2g}) orbital compared to in MoN, and further confirming that there are extra N atoms in the Mo metal lattice.

In order to obtain an in-depth understanding of the changes at the atomic level, the electronic structures of MoN and Mo₅N₆ for Mo 3d and N 2p orbitals were analyzed by DOS calculations (Figure 3d). It can be seen that the different N content greatly affects the electronic environment of Mo–N bonding with more complicated electron orbital hybridization in Mo₅N₆, which is in accordance with the experimental XANES data shown in Figure 3c. Figure 3e shows the total DOS of Mo₅N₆ with a continuous distribution near the Fermi level, indicating its metallic character. It should be noted that the electron hybridization of MoN and Mo₅N₆ are quite different, which may change their d band positions and catalytic performances. For example, the calculated d band center position for Mo₅N₆ is located at –1.96 eV, which is closer to the d band center of Pt (–2.28 eV) compared to MoN (–1.75 eV), indicating an electronic structure more like Pt (Figure S6). It should be noted that the d band center and hydrogen binding energy of electrocatalysts exhibit a linear relationship.³⁴ Consequently, the inherent electronic structure of Mo₅N₆ and the high valence state of its Mo atoms is potentially favorable for high catalytic activity and good stability, respectively.

The electrocatalytic HER performance of Mo₅N₆ was studied in a range of electrolytes (pH 0–14). Figure 4a shows the linear sweep voltammetry (LSV) curves of different catalysts in 1 M KOH. The Mo₅N₆ shows an overpotential of 94 mV at a current density of 10 mA cm⁻², which is significantly lower than that for MoN (389 mV) and close to commercial Pt/C catalysts (21 mV; Figure S7). Furthermore,

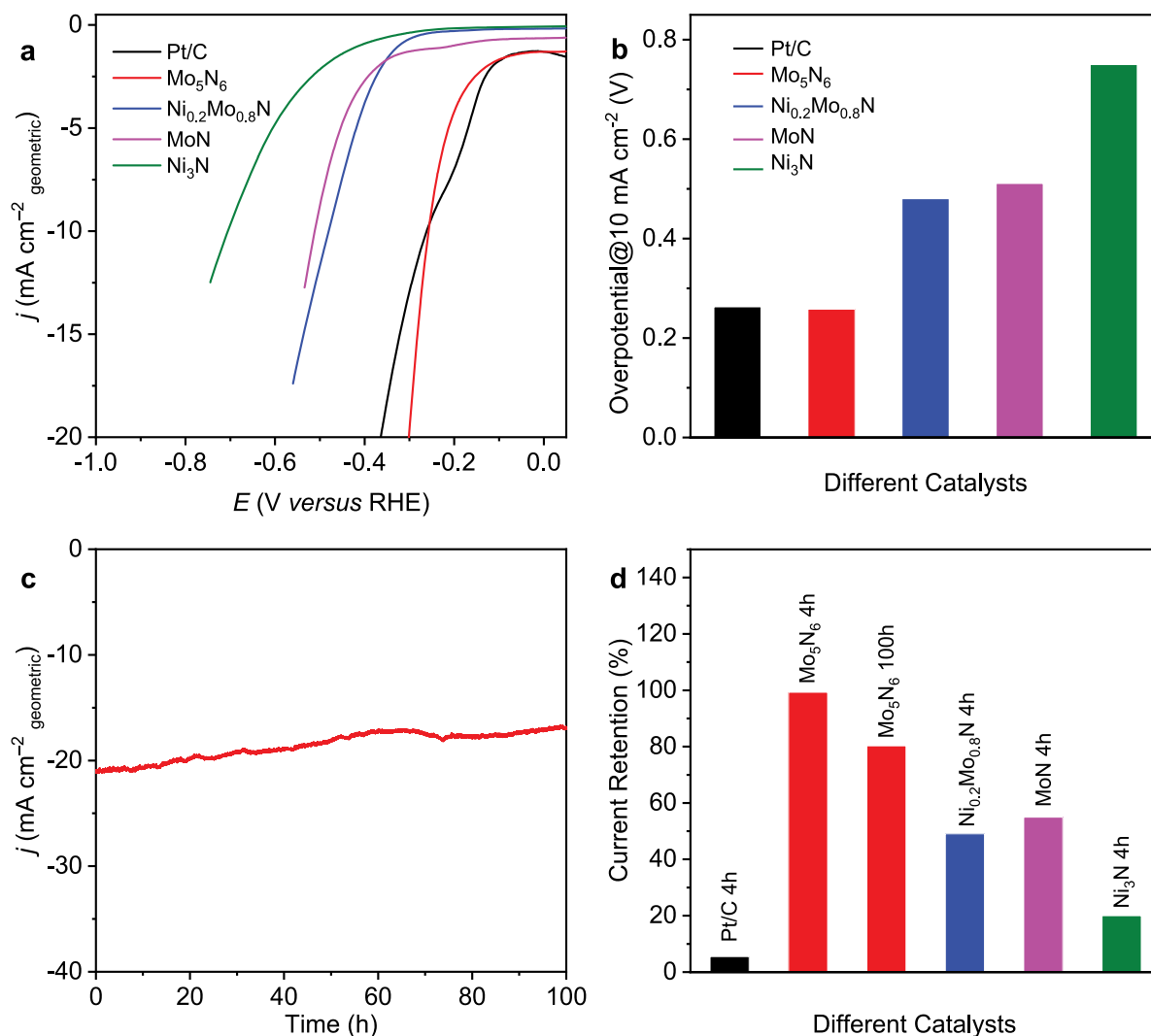


Figure 5. (a) LSV curves of different catalysts measured in Ar-saturated natural seawater. (b) Comparison of overpotentials of Mo₅N₆ with other catalysts at a current density of 10 mA cm⁻². (c) Chronoamperometric curve of Mo₅N₆ over 100 h operation. The applied potential is 310 mV. (d) Comparison of catalytic current retention of Mo₅N₆ with other TMNs and Pt/C in seawater conditions.

we also compared the performance of Mo₅N₆ with other TMN catalysts which are relatively deficient in nitrogen contents. Clearly, the HER performance of Mo₅N₆ is superior than Ni_{0.2}Mo_{0.8}N and Ni₃N individually (Figure S8). Also, Mo₅N₆ shows a Tafel slope of 66 mV dec⁻¹, indicating the sluggish water dissociation is not the rate-determining step in overall HER process. This is also different from other TMNs that have Tafel slopes of ~120 mV dec⁻¹.

Other than in alkaline media, the HER performance of these catalysts was also evaluated in acidic and neutral electrolytes (Figure 4b,c). Similarly, Mo₅N₆ showed the best performance compared to the other TMN catalysts, exhibiting the lowest overpotential in these electrolytes. This pH universal activity enhancement can be attributed to the nitrogen enrichment which altered the d band center position closer to that of Pt and increased the valence state of Mo for optimized water dissociation kinetics. Importantly, Mo₅N₆ shows a smaller electrochemical double-layer capacitance (C_{dl}) than MoN, indicating that the enhanced performance of Mo₅N₆ does not derive from the surface area but from the optimized adsorption energy of key intermediates on the surface (Figures S9 and

S10). Regarding stability, chronoamperometry was carried out for 10 h at a constant overpotential in different electrolytes (Figure 4d–f). Over 10 h, the current response of Mo₅N₆ remained almost unchanged under each operating condition, indicating its very stable performance over a wide range of pH.

On the basis of the above observations, Mo₅N₆ is a highly efficient Pt-like electrocatalyst in alkaline, acid, and neutral electrolytes. Additionally, the nitrogen-rich Mo₅N₆ has high corrosion resistance due to the high valence state of its Mo atoms, making it a promising candidate for natural seawater electrolysis. As expected, Mo₅N₆ exhibited good HER performance in natural seawater, requiring an overpotential of 257 mV to produce 10 mA cm⁻² of catalytic current density. This was lower than that of Pt/C and other nitrogen-deficient TMNs (Figure 5a,b). Further, the j_{10} overpotential (overpotential at current density of 10 mA cm⁻²) on Mo₅N₆ was also lower than most of the non-noble metal catalysts reported for natural seawater HER in the literature (Table S1).^{7,35,36} More importantly, the hydrogen production of Mo₅N₆ in natural seawater was extremely stable for 100 h at an overpotential of 300 mV (Figure 5c). In comparison, the

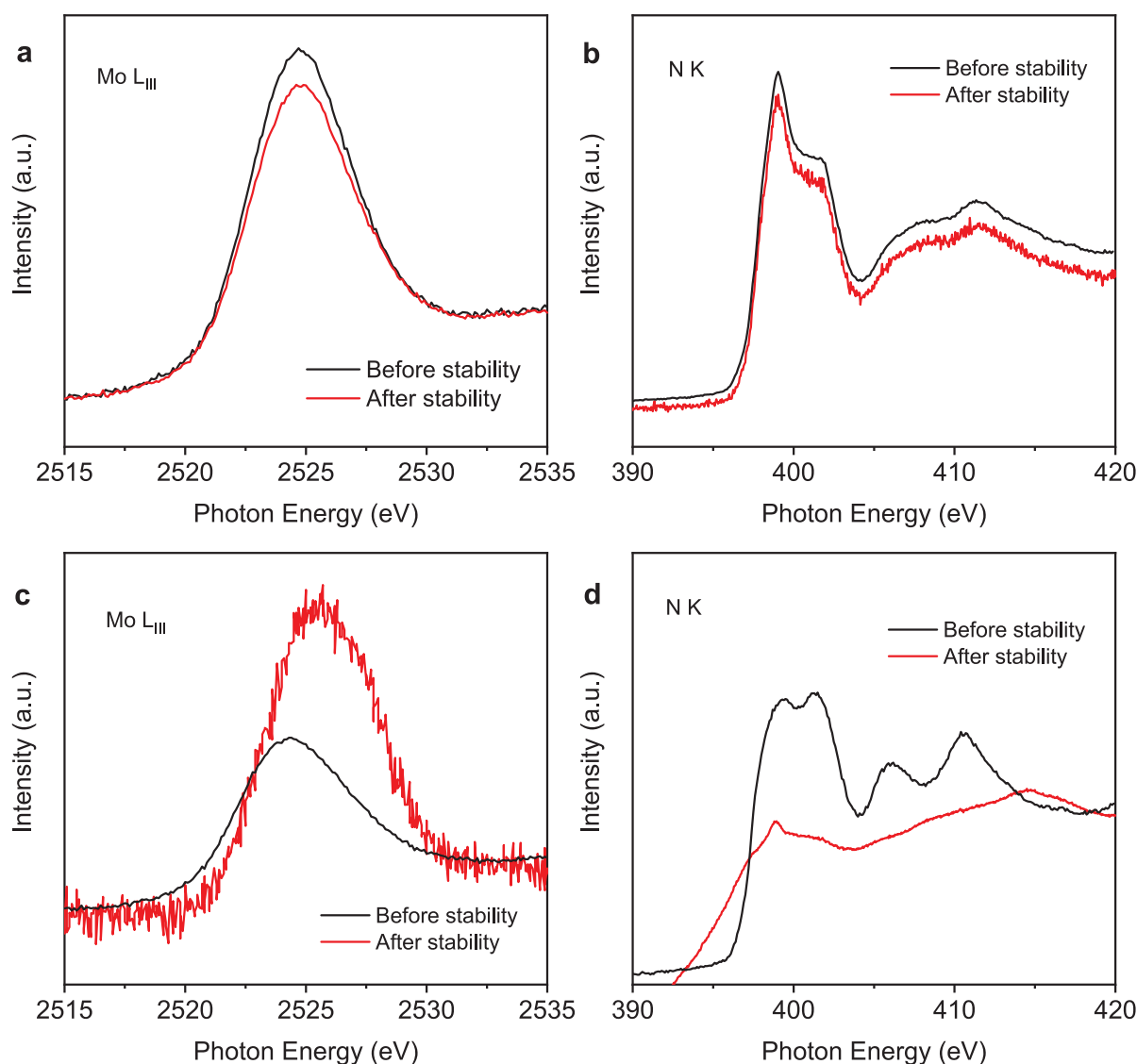


Figure 6. (a,c) Mo L_{III} edge of Mo_5N_6 and MoN before and after stability testing in natural seawater. (b,d) N K edge of Mo_5N_6 and MoN before and after stability testing in natural seawater.

stability of Pt/C was very poor, retaining only 5.5% of its catalytic current density after only 4 h of continuous operation (Figure 5d). This poor stability is likely attributed to the poisoning from ions in seawater which block the active sites for hydrogen evolution, as has been detailed in other works.^{36,37} In addition, Figures 5d and S11 also compare the stability of Mo_5N_6 with other related TMNs. As expected, Mo_5N_6 exhibited high stability with a catalytic current retention of 99.3% after 4 h, which was higher than MoN (55.0% for 4 h), $Ni_{0.2}Mo_{0.8}N$ (49.1% for 4 h), and Ni_3N (20.0% for 4 h), respectively.

To probe the origin of the high stability of Mo_5N_6 in seawater, XRD and XANES of the samples before and after stability testing were carried out. As shown in Figure 6a,b, there was negligible shift for the Mo L_{III} and N K edge of Mo_5N_6 before and after the 100 h stability test in natural seawater, confirming its good resistance to corrosion and poisoning of active sites. From the XRD spectra (Figure S12), it is clear that the crystal structure of Mo_5N_6 was also stable throughout stability testing. In comparison, the structures of

MoN, $Ni_{0.2}Mo_{0.8}N$, and Ni_3N were significantly less stable as evidenced from Figures 6c,d and S13. A positive shift in their XANES spectra indicates that the Mo and Ni valence states of the other TMNs increased. This was likely due to the low valence state of the metal atoms and poor metal–nitrogen bonding making them susceptible to corrosion from the seawater. Furthermore, the significantly different N K-edge XANES spectra of the nitrogen-deficient TMNs indicates disrupted metal–nitrogen bonding. As a result, Mo_5N_6 nanosheets combines the advantages of Pt-like electronic structure and excellent corrosion resistance, resulting ultra-stable performance for hydrogen evolution from seawater.

CONCLUSION

In summary, synthesis of 2D nitrogen-rich Mo_5N_6 nanosheets was successfully achieved using a simple Ni-induced salt-template method. The additional nitrogen atoms incorporated in the Mo_5N_6 lattice greatly changed its inherent properties, leading to a higher Mo valence state and Pt-like electronic structure. As expected, the Mo_5N_6 nanosheet exhibited

excellent HER performance in various electrolytes, especially in seawater. For seawater HER, its performance was significantly better than other nitrogen-deficient TMNs and the Pt/C benchmark. The Mo_3N_6 catalyst combines high activity and good stability simultaneously, demonstrating the possibility of using 2D nitrogen-rich TMNs for electrocatalytic processes in harsh electrocatalytic environments.

METHODS

Synthesis of 2D Mo_3N_6 Nanosheets. The 2D Mo_3N_6 nanosheets were synthesized through a Ni-induced salt-templated method: 0.4 g of Mo powder was dispersed in 40 mL of ethanol with magnetic stirring for 10 min. Then, 1.2 mL of H_2O_2 (30%) solution was injected dropwise into the suspension. After stirring for 12 h at room temperature, the solution turned into a dark blue color. Separately, 10 mg of $\text{Ni}(\text{OCOCH}_3)_2 \cdot 4\text{H}_2\text{O}$ was dissolved in 10 mL of ethanol and mixed with the dark blue suspension to form the precursor. The precursor solution was then mixed with 640 g of NaCl powder and dried at 50 °C with continuous hand stirring. After that, the mixture was annealed at 750 °C for 5 h at a heating rate of 1 °C min^{-1} under a 5% NH_3/Ar atmosphere. Finally, the product was washed with deionized water and dilute hydrochloric acid several times to remove the NaCl template and Ni nanoparticles before being dried using vacuum filtration.

Synthesis of 2D MoN Nanosheets. The 2D MoN nanosheets were synthesized without the addition of Ni. The Mo precursor was mixed with 640 g of NaCl and annealed at 750 °C for 5 h. The final product was obtained by removing NaCl using deionized water and vacuum filtration.

Synthesis of $\text{Ni}_{0.2}\text{Mo}_{0.8}\text{N}$. $\text{Ni}_{0.2}\text{Mo}_{0.8}\text{N}$ was synthesized by adding 0.26 g of $\text{Ni}(\text{OCOCH}_3)_2 \cdot 4\text{H}_2\text{O}$ into the Mo precursor and directly annealing the mixture without the salt-template at 550 °C at a heating rate of 3 °C min^{-1} for 2 h.

Synthesis of Ni_3N . First, $\text{Ni}(\text{OH})_2$ nanosheets were synthesized using a reported method.¹⁴ In a typical procedure, 630 mg of hexamethylenetetramine was dissolved in 100 mL of deionized water and purged with N_2 gas. Then, 120 mg of $\text{NiCl}_2 \cdot 6\text{H}_2\text{O}$ was added to the solution. The reactants were heated under reflux temperature for 12 h with continuous N_2 flow. Light green products were collected from the flask, washed with water and ethanol several times, and freeze-dried for the following steps. Ni_3N was then prepared by annealing $\text{Ni}(\text{OH})_2$ at 390 °C for 2 h at a heating rate of 3 °C min^{-1} under a 5% NH_3/Ar atmosphere.

Characterization. XRD data was collected on a Rigaku MiniFlex 600 X-ray diffractometer. The field-emission scanning electron microscope images were acquired on a FEI Quanta 450 FEG scanning electron microscope. The transmission electron microscope images, aberration-corrected TEM images, high-angle annular dark-field imaging, and EDS data were taken on a FEI Titan Themis 80-200 operating at 200 kV. Atomic force microscopy (AFM, Shimadzu) was used to explore the morphology and thickness of the samples.

The synchrotron-based XPS and XANES measurements were carried out on the soft X-ray spectroscopy beamline at the Australian Synchrotron, which is equipped with a hemispherical electron analyzer and a microchannel plate detector that enables simultaneous recording of the total electron yield and partial electron yield. The raw XANES and XPS data were normalized to the photoelectron current of the photon beam, measured on an Au grid.

Computational Details. Density functional theory calculations were performed using the Vienna *Ab Initio* Simulation Package (VASP).^{38–41} The exchange-correlation interactions were treated within the generalized gradient approximation (GGA) in the form of the Perdew–Burke–Ernzerhof functional.⁴² The van der Waals interactions were described using the empirical correction in Grimme's scheme.⁴³ The electron wave functions were expanded using plane waves with a cutoff energy of 400 eV, and the convergence criteria of energy change during all calculations were set to 10^{-5} eV. The *k*-points were set to be $11 \times 11 \times 1$ for single cells of Mo_3N_6 , MoN, and Pt(111) in density of states calculations. The convergence

tolerance of force on each atom during full structure relaxation was set to be 0.01 eV/Å. To avoid interactions between periodic images, a vacuum space of 20 Å was applied to all calculations.

Electrochemical Measurements. Typically, 4 mg of catalyst (e.g., 2D Mo_3N_6) was dispersed in 800 μL of deionized water. Then 200 μL of 1 wt % of Nafion/water were added to the catalyst dispersion. Because all of the catalysts are electrically conductive, carbon black was not added. Next, 20 μL of catalyst dispersion (4 mg mL^{-1}) was transferred onto a 5 mm glassy carbon rotating disk electrode (0.4 mg cm^{-2}) serving as the working electrode. The reference electrode was Ag/AgCl in 4 M AgCl–KCl solution and the counter electrode was a graphite rod. All potentials were referenced to the reversible hydrogen electrode by adding $(0.205 + 0.059 \times \text{pH})$ and all polarization curves were corrected for the *iR* compensation within the cell. A flow of Ar was maintained over the electrolyte during the experiment to eliminate dissolved oxygen. The working electrode was rotated at 1,600 rpm to remove the hydrogen gas which formed on the catalyst surface. The seawater used in this study was collected from Henley Beach (Adelaide, Australia) with a pH value of ~ 8.4 .

ASSOCIATED CONTENT

Supporting Information

The Supporting Information is available free of charge on the ACS Publications website at DOI: 10.1021/acsnano.8b07841.

Additional figures, table, and references (PDF)

AUTHOR INFORMATION

Corresponding Authors

*E-mail: yao.zheng01@adelaide.edu.au.

*E-mail: s.qiao@adelaide.edu.au.

ORCID

Yan Jiao: 0000-0003-1329-4290

Yao Zheng: 0000-0002-2411-8041

Shi-Zhang Qiao: 0000-0002-4568-8422

Notes

The authors declare no competing financial interest.

ACKNOWLEDGMENTS

This work is financially supported by the Australian Research Council (DP170104464, DP160104866, DE160101163, and FL170100154). We acknowledge Adelaide Microscopy at The University of Adelaide, an AMMRF facility for the microscopy and microanalysis services. We acknowledge the support of ANSTO in providing the XANES and XRD data, which were undertaken on the Soft X-ray Spectroscopy beamline and Powder Diffraction beamline.

REFERENCES

- (1) Seh, Z. W.; Kibsgaard, J.; Dickens, C. F.; Chorkendorff, I.; Nørskov, J. K.; Jaramillo, T. F. Combining Theory and Experiment in Electrocatalysis: Insights into Materials Design. *Science* **2017**, 355, No. eaad4998.
- (2) Gasteiger, H. A.; Marković, N. M. Just a Dream—or Future Reality? *Science* **2009**, 324, 48–49.
- (3) Jin, H.; Guo, C.; Liu, X.; Liu, J.; Vasileff, A.; Jiao, Y.; Zheng, Y.; Qiao, S.-Z. Emerging Two-Dimensional Nanomaterials for Electrocatalysis. *Chem. Rev.* **2018**, 118, 6337–6408.
- (4) Hu, C.; Ma, Q.; Hung, S.-F.; Chen, Z.-N.; Ou, D.; Ren, B.; Chen, H. M.; Fu, G.; Zheng, N. *In Situ* Electrochemical Production of Ultrathin Nickel Nanosheets for Hydrogen Evolution Electrocatalysis. *Chem.* **2017**, 3, 122–133.
- (5) Chen, Z.; Song, Y.; Cai, J.; Zheng, X.; Han, D.; Wu, Y.; Zang, Y.; Niu, S.; Liu, Y.; Zhu, J.; Liu, X.; Wang, G. Tailoring the d-Band

Centers Enables Co₄N Nanosheets to Be Highly Active for Hydrogen Evolution Catalysis. *Angew. Chem.* **2018**, *130*, 5170–5174.

(6) Zhang, J.; Wang, T.; Pohl, D.; Rellinghaus, B.; Dong, R.; Liu, S.; Zhuang, X.; Feng, X. Interface Engineering of MoS₂/Ni₃S₂ Heterostructures for Highly Enhanced Electrochemical Overall-Water-Splitting Activity. *Angew. Chem.* **2016**, *128*, 6814–6819.

(7) Lu, X.; Pan, J.; Lovell, E.; Tan, T. H.; Ng, Y. H.; Amal, R. A Sea-Change: Manganese Doped Nickel/Nickel Oxide Electrocatalysts for Hydrogen Heneration from Seawater. *Energy Environ. Sci.* **2018**, *11*, 1898.

(8) Zhao, Y.; Jin, B.; Zheng, Y.; Jin, H.; Jiao, Y.; Qiao, S.-Z. Charge State Manipulation of Cobalt Selenide Catalyst for Overall Seawater Electrolysis. *Adv. Energy Mater.* **2018**, *8*, 1801926.

(9) Bennett, J. E. Electrodes for Generation of Hydrogen and Oxygen from Seawater. *Int. J. Hydrogen Energy* **1980**, *5*, 401–408.

(10) Wang, Y.; Chen, L.; Yu, X.; Wang, Y.; Zheng, G. Superb Alkaline Hydrogen Evolution and Simultaneous Electricity Generation by Pt-Decorated Ni₃N Nanosheets. *Adv. Energy Mater.* **2017**, *7*, 1601390.

(11) Jin, H.; Zhang, H.; Chen, J.; Mao, S.; Jiang, Z.; Wang, Y. A General Synthetic Approach for Hexagonal Phase Tungsten Nitride Composites and Their Application in the Hydrogen Evolution Reaction. *J. Mater. Chem. A* **2018**, *6*, 10967–10975.

(12) Xiong, J.; Cai, W.; Shi, W.; Zhang, X.; Li, J.; Yang, Z.; Feng, L.; Cheng, H. Salt-Templated Synthesis of Defect-Rich MoN Nanosheets for Boosted Hydrogen Evolution Reaction. *J. Mater. Chem. A* **2017**, *5*, 24193–24198.

(13) Xie, J.; Li, S.; Zhang, X.; Zhang, J.; Wang, R.; Zhang, H.; Pan, B.; Xie, Y. Atomically-Thin Molybdenum Nitride Nanosheets with Exposed Active Surface Sites for Efficient Hydrogen Evolution. *Chem. Sci.* **2014**, *5*, 4615–4620.

(14) Xu, K.; Chen, P.; Li, X.; Tong, Y.; Ding, H.; Wu, X.; Chu, W.; Peng, Z.; Wu, C.; Xie, Y. Metallic Nickel Nitride Nanosheets Realizing Enhanced Electrochemical Water Oxidation. *J. Am. Chem. Soc.* **2015**, *137*, 4119–4125.

(15) Xie, J.; Xie, Y. Transition Metal Nitrides for Electrocatalytic Energy Conversion: Opportunities and Challenges. *Chem. - Eur. J.* **2016**, *22*, 3588–3598.

(16) Chen, J. G. Carbide and Nitride Overlayers on Early Transition Metal Surfaces: Preparation, Characterization, and Reactivities. *Chem. Rev.* **1996**, *96*, 1477–1498.

(17) Wang, S.; Ge, H.; Sun, S.; Zhang, J.; Liu, F.; Wen, X.; Yu, X.; Wang, L.; Zhang, Y.; Xu, H.; Neuefeind, J. C.; Qin, Z.; Chen, C.; Jin, C.; Li, Y.; He, D.; Zhao, Y. A New Molybdenum Nitride Catalyst with Rhombohedral MoS₂ Structure for Hydrogenation Applications. *J. Am. Chem. Soc.* **2015**, *137*, 4815–4822.

(18) Salamat, A.; Hector, A. L.; Kroll, P.; McMillan, P. F. Nitrogen-Rich Transition Metal Nitrides. *Coord. Chem. Rev.* **2013**, *257*, 2063–2072.

(19) Wang, S.; Yu, X.; Lin, Z.; Zhang, R.; He, D.; Qin, J.; Zhu, J.; Han, J.; Wang, L.; Mao, H.-k.; Zhang, J.; Zhao, Y. Synthesis, Crystal Structure, and Elastic Properties of Novel Tungsten Nitrides. *Chem. Mater.* **2012**, *24*, 3023–3028.

(20) Bykov, M.; Bykova, E.; Aprilis, G.; Glazyrin, K.; Koemets, E.; Chuvashova, I.; Kupenko, I.; McCammon, C.; Mezouar, M.; Prakash, V.; Liermann, H. P.; Tasnádi, F.; Ponomareva, A. V.; Abrikosov, I. A.; Dubrovinskaya, N.; Dubrovinsky, L. Fe-N System at High Pressure Reveals a Compound Featuring Polymeric Nitrogen Chains. *Nat. Commun.* **2018**, *9*, 2756.

(21) Xiao, X.; Yu, H.; Jin, H.; Wu, M.; Fang, Y.; Sun, J.; Hu, Z.; Li, T.; Wu, J.; Huang, L.; Gogotsi, Y.; Zhou, J. Salt-Templated Synthesis of 2D Metallic MoN and Other Nitrides. *ACS Nano* **2017**, *11*, 2180–2186.

(22) Anasori, B.; Lukatskaya, M. R.; Gogotsi, Y. 2D Metal Carbides and Nitrides (MXenes) for Energy Storage. *Nat. Rev. Mater.* **2017**, *2*, 16098.

(23) Jaramillo, T. F.; Jørgensen, K. P.; Bonde, J.; Nielsen, J. H.; Hørch, S.; Chorkendorff, I. Identification of Active Edge Sites for

Electrochemical H₂ Evolution from MoS₂ Nanocatalysts. *Science* **2007**, *317*, 100.

(24) Voiry, D.; Yamaguchi, H.; Li, J.; Silva, R.; Alves, D. C. B.; Fujita, T.; Chen, M.; Asefa, T.; Shenoy, V. B.; Eda, G.; Chhowalla, M. Enhanced Catalytic Activity in Strained Chemically Exfoliated WS₂ Nanosheets for Hydrogen Evolution. *Nat. Mater.* **2013**, *12*, 850–855.

(25) Yang, W.; Zhang, X.; Xie, Y. Advances and Challenges in Chemistry of Two-Dimensional Nanosheets. *Nano Today* **2016**, *11*, 793–816.

(26) Ganin, A. Y.; Kienle, L.; Vajenine, G. V. Synthesis and Characterisation of Hexagonal Molybdenum Nitrides. *J. Solid State Chem.* **2006**, *179*, 2339–2348.

(27) Sun, G.-D.; Zhang, G.-H.; Chou, K.-C. Synthesis of Molybdenum Nitrides Nanosheets by Nitriding 2H-MoS₂ with Ammonia. *J. Am. Ceram. Soc.* **2018**, *101*, 2796–2808.

(28) Yu, H.; Yang, X.; Xiao, X.; Chen, M.; Zhang, Q.; Huang, L.; Wu, J.; Li, T.; Chen, S.; Song, L.; Gu, L.; Xia, B. Y.; Feng, G.; Li, J.; Zhou, J. Atmospheric-Pressure Synthesis of 2D Nitrogen-Rich Tungsten Nitride. *Adv. Mater.* **2018**, 1805655.

(29) Xiao, X.; Song, H.; Lin, S.; Zhou, Y.; Zhan, X.; Hu, Z.; Zhang, Q.; Sun, J.; Yang, B.; Li, T.; Jiao, L.; Zhou, J.; Tang, J.; Gogotsi, Y. Scalable Salt-Templated Synthesis of Two-Dimensional Transition Metal Oxides. *Nat. Commun.* **2016**, *7*, 11296.

(30) Jin, H.; Liu, X.; Jiao, Y.; Vasileff, A.; Zheng, Y.; Qiao, S.-Z. Constructing Tunable Dual Active Sites on Two-Dimensional C₃N₄@MoN Hybrid for Electrocatalytic Hydrogen Evolution. *Nano Energy* **2018**, *53*, 690–697.

(31) Staszak-Jirkovsky, J.; Malliakas, C. D.; Lopes, P. P.; Danilovic, N.; Kota, S. S.; Chang, K. C.; Genorio, B.; Strmcnik, D.; Stamenkovic, V. R.; Kanatzidis, M. G.; Markovic, N. M. Design of Active and Stable Co-Mo-S_x Chalcogenides as pH-Universal Catalysts for the Hydrogen Evolution Reaction. *Nat. Mater.* **2016**, *15*, 197–203.

(32) Bennett, L. H.; Cuthill, J. R.; McAlister, A. J.; Erickson, N. E.; Watson, R. E. Electronic Structure and Catalytic Behavior of Tungsten Carbide. *Science* **1974**, *184*, 563.

(33) Kapoor, R.; Oyama, S. T.; Friihberger, B.; DeVries, B. D.; Chen, J. G. Characterization of Early Transition Metal Carbides and Nitrides by NEXAFS. *Catal. Lett.* **1995**, *34*, 179–189.

(34) Jiao, Y.; Zheng, Y.; Jaroniec, M.; Qiao, S. Z. Design of Electrocatalysts for Oxygen- and Hydrogen-Involving Energy Conversion Reactions. *Chem. Soc. Rev.* **2015**, *44*, 2060–2086.

(35) Gao, S.; Li, G.-D.; Liu, Y.; Chen, H.; Feng, L.-L.; Wang, Y.; Yang, M.; Wang, D.; Wang, S.; Zou, X. Electrocatalytic H₂ Production from Seawater Over Co, N-Codoped Nanocarbons. *Nanoscale* **2015**, *7*, 2306–2316.

(36) Ma, Y.-Y.; Wu, C.-X.; Feng, X.-J.; Tan, H.-Q.; Yan, L.-K.; Liu, Y.; Kang, Z.-H.; Wang, E.-B.; Li, Y.-G. Highly Efficient Hydrogen Evolution from Seawater by a Low-Cost and Stable CoMoP@C Electrocatalyst Superior to Pt/C. *Energy Environ. Sci.* **2017**, *10*, 788–798.

(37) Hsu, S. H.; Miao, J.; Zhang, L.; Gao, J.; Wang, H.; Tao, H.; Hung, S. F.; Vasileff, A.; Qiao Shi, Z.; Liu, B. An Earth-Abundant Catalyst-Based Seawater Photoelectrolysis System with 17.9% Solar-to-Hydrogen Efficiency. *Adv. Mater.* **2018**, *30*, 1707261.

(38) Kresse, G.; Furthmüller, J. Efficiency of *ab-initio* Total Energy Calculations for Metals and Semiconductors using a Plane-Wave Basis Set. *Comput. Mater. Sci.* **1996**, *6*, 15–50.

(39) Kresse, G.; Furthmüller, J. Efficient Iterative Schemes for *ab initio* Total-Energy Calculations Using a Plane-Wave Basis Set. *Phys. Rev. B: Condens. Matter Mater. Phys.* **1996**, *54*, 11169–11186.

(40) Kresse, G.; Hafner, J. *Ab initio* Molecular Dynamics for Liquid Metals. *Phys. Rev. B: Condens. Matter Mater. Phys.* **1993**, *47*, 558–561.

(41) Kresse, G.; Hafner, J. *Ab initio* Molecular-Dynamics Simulation of the Liquid-Metal–Amorphous-Semiconductor Transition in Germanium. *Phys. Rev. B: Condens. Matter Mater. Phys.* **1994**, *49*, 14251–14269.

(42) Perdew, J. P.; Burke, K.; Ernzerhof, M. Generalized Gradient Approximation Made Simple. *Phys. Rev. Lett.* **1996**, *77*, 3865–3868.

(43) Grimme, S. Semiempirical GGA-Type Density Functional Constructed with a Long-Range Dispersion Correction. *J. Comput. Chem.* **2006**, *27*, 1787–1799.